

Nuclear pasta and symmetry energy in the relativistic point-coupling model

Fan Ji^①,¹ Jinniu Hu^②,^{1,*} and Hong Shen^③,^{1,†}

¹*School of Physics, Nankai University, Tianjin 300071, China*

Nonuniform structure of low-density nuclear matter, known as nuclear pasta, is expected to appear not only in the inner crust of neutron stars but also in core-collapse supernova explosions and neutron-star mergers. We perform fully three-dimensional calculations of inhomogeneous nuclear matter and neutron-star matter in the low-density region using the Thomas-Fermi approximation. The nuclear interaction is described in the relativistic mean-field approach with the point-coupling interaction, where the meson exchange in each channel is replaced by the contact interaction between nucleons. We investigate the influence of nuclear symmetry energy and its density dependence on pasta structures by introducing a coupling term between the isoscalar-vector and isovector-vector interactions. It is found that the properties of pasta phases in the neutron-rich matter are strongly dependent on the symmetry energy and its slope. In addition to typical shapes like droplets, rods, slabs, tubes, and bubbles, some intermediate pasta structures are also observed in cold stellar matter with a relatively large proton fraction. We find that nonspherical shapes are unlikely to be formed in neutron-star crusts, since the proton fraction obtained in β equilibrium is rather small. The inner crust properties may lead to a visible difference in the neutron-star radius.

I. INTRODUCTION

A core-collapse supernova explosion is one of the most spectacular events in the universe, which marks the violent death of a massive star. After the explosion, it leaves behind either a neutron star or a black hole depending on its mass [1–3]. Nuclear matter in supernovae and neutron stars covers a wide range of baryon density, temperature, and isospin asymmetry [4, 5]. In the interior of neutron stars, the uniform matter is highly isospin asymmetric, while its baryon density may be as high as several times nuclear saturation density ρ_0 . From the inside to the outside of a neutron star, the matter density decreases to subnuclear region and the core-crust transition occurs when homogeneous matter becomes unstable against the formation of nuclear clusters. It is believed that a neutron star consists of an inner crust of nuclei in a gas of neutrons and electrons, as well as an outer crust of nuclei in a gas of electrons without dripped neutrons [6–8]. The inner crust of neutron stars has attracted much attention due to its complex phase structure and important role in astrophysical observations [9–14]. With increasing density in the inner crust, spherical nuclei become unstable and the favored geometric shape may change from droplet to rod, slab, tube, and bubble before the crust-core transition. These exotic nuclear shapes are known as pasta phases, which are expected to appear not only in the inner crust of neutron stars but also in core-collapse supernova explosions and neutron-star mergers. In warm stellar matter relevant for supernovae, light clusters like α particles and deuterons may be formed before the formation of heavy nuclei and nuclear pasta [4, 5, 15]. It

has been found that the presence of nuclear pasta in core-collapse supernovae could alter the late-time neutrino signal and affect the evolution of a protoneutron star [16, 17]. The elastic properties of nuclear pasta are currently interesting to some researchers for their relevance to the gravitational-wave searches from supernovae and neutron-star mergers [18–21].

During the last decades, the properties of pasta phases have been studied by using various methods, such as the liquid-drop model [9, 15, 22, 23] and the Thomas-Fermi approximation [11, 12, 24–28]. In these calculations, the Wigner-Seitz approximation was generally employed, where typical geometric shapes of nuclear pasta were assumed in order to simplify the calculations. However, the assumption of geometric symmetry would artificially reduce the configuration space, and as a result, other possible pasta shapes besides the typical structures may be missed. For a more realistic description of pasta phases, there are some studies that have not explicitly assumed any geometric shape and performed fully three-dimensional calculations for nuclear pasta based on the Thomas-Fermi approximation [13, 29, 30], Hartree-Fock approach [14, 31–35], and molecular dynamics method [36–41]. In these calculations, not only the typical pasta shapes assumed in the Wigner-Seitz approximation were reproduced but also other complex structures such as the waffle phase were reported [14, 41].

The properties of pasta phases appearing in the inner crust of neutron stars can be significantly influenced by the nuclear symmetry energy and its density dependence [11, 12, 25]. In recent years, the symmetry energy has received great interest due to its importance for understanding many phenomena in nuclear physics and astrophysics [4, 42, 43]. It has been shown that the properties of neutron stars, such as the radius and the crust structure, are sensitive to the symmetry energy E_{sym} and its slope parameter L [11, 12, 25, 44–50]. Great efforts

*Electronic address: hujinniu@nankai.edu.cn

†Electronic address: shennankai@gmail.com

have been devoted to constraining the values of E_{sym} and L based on astrophysical observations and terrestrial nuclear experiments [51–57]. In Ref. [4], a sufficient number of constraints on the symmetry energy parameters have been summarized, and the most probable values for the symmetry energy and its slope at saturation density were found to be $E_{\text{sym}} = 31.7 \pm 3.2$ MeV and $L = 58.7 \pm 28.1$ MeV, respectively, with a much larger error for L than that for E_{sym} .

The first detection of gravitational waves from a binary neutron-star merger, known as GW170817, provides valuable constraints on the tidal deformability [58–60], which also restricts the radii of neutron stars [61–65]. More recently, the gravitational-wave events, GW190425 [66] and GW190814 [67], were reported by the LIGO and Virgo Collaborations, which may give important information for the equation of state (EOS) of dense matter. The recent observation by the Neutron Star Interior Composition Explorer (NICER) provided a simultaneous measurement of the mass and radius for PSR J0030+0451 [68, 69]. These exciting developments in astrophysical observations suggest relatively small radii of neutron stars, which is likely to favor a small value of the symmetry energy slope L . It is well known that there is a strong correlation between the symmetry energy slope and the neutron-star radius [47, 70]. Furthermore, other properties of neutron stars, such as the crust structure and the crust-core transition, are also directly affected by the symmetry energy and its slope [11, 12, 25]. In Ref. [25], the density region of nonspherical nuclei was calculated by using a parametrized Thomas-Fermi approximation, which was found to be sensitive to the symmetry energy slope L . In our previous work [12], a self-consistent Thomas-Fermi approximation was employed to study the pasta structures presented in the inner crust of neutron stars and we found that only spherical nuclei can be formed before the crust-core transition for $L \geq 80$ MeV, whereas nonspherical pasta phases may appear for smaller values of L (e.g., $L = 40$ MeV). A similar calculation using the coexisting phases method in the quark-meson coupling model with $L = 69$ and 90 MeV was performed and showed that only droplets could present in the inner crust of neutron stars [71].

It is interesting to clarify the correlation between the symmetry energy slope and nuclear pasta structures. In the present work, we perform fully three-dimensional calculations without any assumption about the pasta shapes. We carry out the calculation in a cubic box with periodic boundary conditions. The pasta phase presented in neutron-star crusts is highly isospin asymmetric matter in β equilibrium, whereas the one occurred in supernovae is less asymmetric and out of β equilibrium. Therefore, we investigate the pasta structures for stellar matter with a fixed proton fraction and neutron-star matter in β equilibrium. In this study, all calculations are carried out at zero temperature for simplicity. It is known that nonuniform structure in supernova matter exists at low temperatures ($T < 15$ MeV) [4, 5, 72], but

the three-dimensional calculations at finite temperature require much more computational time. For the nuclear interaction, we employ the relativistic mean-field model with point-coupling force (RMF-PC), which has achieved great success in describing various phenomena in nuclear physics over the past decades [73–84]. In the RMF-PC approach, the finite-range interactions through meson exchange in Walecka-type models are replaced by corresponding zero-range interactions (point-coupling) together with derivative terms. In the present work, we use the PC-PK1 parametrization proposed by Zhao *et al.* [80], which was determined by fitting to observables of 60 selected spherical nuclei and provides a good description of ground-state properties for the nuclei all over the nuclear chart [82–84]. In order to examine the effect of the symmetry energy slope L on nuclear pasta structures, we generate a set of models with different values of L at saturation density based on the PC-PK1 parametrization by introducing an additional coupling term between the isoscalar-vector and isovector-vector interactions, which corresponds to the ω - ρ coupling in the finite-range RMF models [85]. It has been found that this term plays a crucial role in determining the density dependence of the symmetry energy and affecting neutron-star properties [12, 23, 45, 46, 85–88]. By adjusting two parameters simultaneously, a given slope L at saturation density ρ_0 can be achieved and the symmetry energy E_{sym} at average nuclear density $\rho_B = 0.12 \text{ fm}^{-3}$ is fixed to the value predicted by the original PC-PK1 parametrization. We note that all models in the set have the same isoscalar properties and a fixed symmetry energy at $\rho_B = 0.12 \text{ fm}^{-3}$, but they have different symmetry energy slope L . The difference of L does not significantly affect the properties of stable nuclei except the neutron-skin thickness. Therefore, the set of models can provide very similar description of finite nuclei and symmetric nuclear matter. It is helpful to use these models to study the impact of the symmetry energy slope L on nuclear pasta structures at subnuclear densities.

This article is organized as follows. In Sec. II, we briefly describe the RMF-PC model employed in the three-dimensional calculations of nuclear pasta phases. In Sec. III, we discuss the model parameters used in this study. In Sec. IV, we present the numerical results and discuss the effects of the symmetry energy and its slope on pasta structures. Sec. V is devoted to the conclusions.

II. FORMALISM

The nonuniform matter at subnuclear densities is studied within the Thomas-Fermi approximation. Generally, the Wigner-Seitz approximation with several typical geometric shapes is employed in the Thomas-Fermi calculation of nuclear pasta phases, where the assumed geometric symmetry can help simplify the calculation to a one-dimensional problem, but it artificially reduces the configuration space. In the present work, we prefer to

perform fully three-dimensional calculations without any assumption about the geometric symmetry. The calculation is carried out in a large cubic cell where the periodic boundary condition is used. The nucleons in the cell tend to form clusters in order to lower the free energy of the system. The electrons are assumed to be uniformed in the cell for simplicity, since the electron screening effect caused by its nonuniform distribution is relatively small at subnuclear densities [89].

For the nuclear interaction, we employ the RMF-PC approach, where the finite-range interactions through meson exchange are replaced by corresponding zero-range interactions together with derivative terms. For a system of nucleons and electrons, the Lagrangian density of the RMF-PC model reads

$$\begin{aligned}
\mathcal{L} = & \bar{\psi} (i\gamma_\mu \partial^\mu - m_N) \psi + \bar{\psi}_e (i\gamma_\mu \partial^\mu - m_e) \psi_e \\
& - \frac{1}{2} \alpha_S (\bar{\psi}\psi) (\bar{\psi}\psi) - \frac{1}{2} \alpha_V (\bar{\psi}\gamma_\mu\psi) (\bar{\psi}\gamma^\mu\psi) \\
& - \frac{1}{2} \alpha_{TV} (\bar{\psi}\vec{\tau}\gamma_\mu\psi) (\bar{\psi}\vec{\tau}\gamma^\mu\psi) - \frac{1}{3} \beta_S (\bar{\psi}\psi)^3 \\
& - \frac{1}{4} \gamma_S (\bar{\psi}\psi)^4 - \frac{1}{4} \gamma_V [(\bar{\psi}\gamma_\mu\psi) (\bar{\psi}\gamma^\mu\psi)]^2 \\
& - \gamma_C [(\bar{\psi}\gamma_\mu\psi) (\bar{\psi}\gamma^\mu\psi)] [(\bar{\psi}\vec{\tau}\gamma_\mu\psi) (\bar{\psi}\vec{\tau}\gamma^\mu\psi)] \\
& - \frac{1}{2} \delta_S \partial_\nu (\bar{\psi}\psi) \partial^\nu (\bar{\psi}\psi) - \frac{1}{2} \delta_V \partial_\nu (\bar{\psi}\gamma_\mu\psi) \partial^\nu (\bar{\psi}\gamma^\mu\psi) \\
& - \frac{1}{2} \delta_{TV} \partial_\nu (\bar{\psi}\vec{\tau}\gamma_\mu\psi) \partial^\nu (\bar{\psi}\vec{\tau}\gamma^\mu\psi) - \frac{1}{4} F^{\mu\nu} F_{\mu\nu} \\
& - e \frac{1-\tau_3}{2} \bar{\psi}\gamma_\mu\psi A^\mu + e \bar{\psi}_e \gamma_\mu \psi_e A^\mu, \tag{1}
\end{aligned}$$

where m_N and m_e are the nucleon and electron masses, respectively. A^μ is the four-vector potential of the electromagnetic field with $F^{\mu\nu}$ being its antisymmetric field tensor. The interactions include four-fermion terms with coupling constants α , while β and γ refer to third- and fourth-order terms, respectively. The interactions with δ contain the derivative couplings. The subscripts S , V , and TV refer to isoscalar-scalar, isoscalar-vector, and isovector-vector respectively, which correspond to the exchange of σ , ω , and ρ mesons in the finite-range RMF models. We employ the PC-PK1 parametrization proposed in Ref. [80], where the isovector-scalar channel (δ meson) is neglected since the inclusion of the isovector-scalar interactions generally does not help improve the description of ground state properties of stable nuclei. Attempts to include the isovector-scalar interactions in Ref. [75] show that the addition of isovector-scalar terms does not incorporate real physical improvements and is not required for a viable description of the strong interaction in finite nuclei. In order to study the influence of nuclear symmetry energy, we introduce an additional coupling (γ_C) between the isoscalar-vector and isovector-vector interactions based on the PC-PK1 parametrization, which plays a crucial role in modifying the density dependence of nuclear symmetry energy.

In the mean-field approximation, the interactions in the Lagrangian density are replaced by their expectation

values, which can be expressed in terms of corresponding local densities. The energy density functional of the system is derived from the energy-momentum tensor. By using standard variational techniques, one can obtain the Dirac equation for the nucleon,

$$\begin{aligned}
& \left[-i\alpha \cdot \nabla + \beta (m_N + V_S) + V_V + \tau_3 V_{TV} \right. \\
& \left. + e \frac{1-\tau_3}{2} A \right] \psi_k = \epsilon_k \psi_k, \tag{2}
\end{aligned}$$

where the potentials are given by the following relations:

$$V_S = \alpha_S \rho_S + \beta_S \rho_S^2 + \gamma_S \rho_S^3 + \delta_S \Delta \rho_S, \tag{3}$$

$$V_V = \alpha_V \rho_V + \gamma_V \rho_V^3 + \delta_V \Delta \rho_V + 2\gamma_C \rho_V \rho_{TV}^2, \tag{4}$$

$$V_{TV} = \alpha_{TV} \rho_{TV} + \delta_{TV} \Delta \rho_{TV} + 2\gamma_C \rho_V^2 \rho_{TV}, \tag{5}$$

with $\rho_S(\mathbf{r})$, $\rho_V(\mathbf{r})$, and $\rho_{TV}(\mathbf{r})$ being the local densities in scalar, vector, and isovector-vector channels, respectively. $\Delta \rho_S$, $\Delta \rho_V$, and $\Delta \rho_{TV}$ are the corresponding derivative terms, where Δ is the Laplace operator. We use the nuclear physics convention for the isospin, i.e., the neutron is associated with $\tau_3 = +1$ and the proton with $\tau_3 = -1$. In the Thomas-Fermi approximation, the chemical potentials of nucleons are expressed as

$$\mu_p = \sqrt{k_F^p{}^2 + m_N^*{}^2} + V_V - V_{TV} + eA, \tag{6}$$

$$\mu_n = \sqrt{k_F^n{}^2 + m_N^*{}^2} + V_V + V_{TV}, \tag{7}$$

where $m_N^*(\mathbf{r}) = m_N + V_S(\mathbf{r})$ is the effective nucleon mass and $k_F^i(\mathbf{r})$ is the Fermi momentum. We emphasize that the chemical potential is spatially constant throughout the whole system, while other quantities such as various densities depend on the position \mathbf{r} . The electrostatic potential $A(\mathbf{r})$ satisfies the Poisson equation

$$\Delta A(\mathbf{r}) = -e [\rho_V^p(\mathbf{r}) - \rho_V^n(\mathbf{r})], \tag{8}$$

where the electron number density ρ_V^e is assumed to be uniform in the system for simplicity.

For nonuniform matter at a given average baryon density ρ_B and fixed proton fraction Y_p , the most stable state is the one with the lowest energy. We calculate the energy of a large cubic cell by performing the three-dimensional integration,

$$E = \int d^3r \varepsilon(\mathbf{r}), \tag{9}$$

where the local energy density within the Thomas-Fermi

approximation is given by

$$\begin{aligned}
\varepsilon(\mathbf{r}) = & \sum_{b=p,n} \frac{1}{\pi^2} \int_0^{k_F^b} dk k^2 \sqrt{k^2 + m_N^{*2}} \\
& - \frac{1}{2} \alpha_S \rho_S^2 - \frac{1}{2} \delta_S \rho_S \Delta \rho_S - \frac{2}{3} \beta_S \rho_S^3 \\
& - \frac{3}{4} \gamma_S \rho_S^4 + \frac{1}{2} \alpha_V \rho_V^2 + \frac{1}{2} \delta_V \rho_V \Delta \rho_V \\
& + \frac{1}{4} \gamma_V \rho_V^4 + \frac{1}{2} \alpha_{TV} \rho_{TV}^2 + \frac{1}{2} \delta_{TV} \rho_{TV} \Delta \rho_{TV} \\
& + \frac{1}{2} eA (\rho_V^p - \rho_V^n) + \gamma_C \rho_V^p \rho_{TV}^n \\
& + \frac{1}{\pi^2} \int_0^{k_F^e} dk k^2 \sqrt{k^2 + m_e^2}. \quad (10)
\end{aligned}$$

We use the iteration method to solve this problem. In practice, we start with an initial guess for all density distributions $\rho_S(\mathbf{r})$, $\rho_V(\mathbf{r})$, $\rho_{TV}(\mathbf{r})$, and the electrostatic potential $A(\mathbf{r})$. Then, the chemical potentials, μ_p and μ_n , are respectively determined by given proton and neutron numbers inside the cell. Once the chemical potentials are achieved, the new Fermi momentum, $k_F^p(\mathbf{r})$ and $k_F^n(\mathbf{r})$, can be obtained from the relations (6) and (7), which result in new density distributions. Furthermore, new $A(\mathbf{r})$ is obtained by solving the Poisson equation. This procedure should be iterated until convergence is achieved.

III. PARAMETERS

The parameters of the RMF-PC models are generally determined by fitting to the ground-state properties of finite nuclei. Several successful RMF-PC parametrizations have been proposed and widely used in describing various nuclear properties [74, 75, 78, 80, 83, 84]. In the present work, we employ the PC-PK1 parametrization proposed by Zhao *et al.* [80], which was determined by fitting to observables of 60 selected spherical nuclei, including the binding energies, charge radii, and empirical pairing gaps. The PC-PK1 parametrization provides satisfactory description for both spherical and deformed nuclei throughout the nuclear chart [84]. For completeness, we present the PC-PK1 parametrization of the RMF-PC model in Table I. With the PC-PK1 parametrization, the predicted saturation properties of nuclear matter are as follows: the saturation density $\rho_0 = 0.153 \text{ fm}^{-3}$, energy per nucleon $E_0 = -16.12 \text{ MeV}$, incompressibility $K = 238 \text{ MeV}$, symmetry energy $E_{\text{sym}} = 35.6 \text{ MeV}$, and the slope of symmetry energy $L = 113 \text{ MeV}$. Due to the large value of L , the PC-PK1 parametrization of the RMF-PC model predicts rather large radii and tidal deformabilities of neutron stars [90], which are disfavored by recent astrophysical observations as discussed in the introduction. The inclusion of a coupling term between the isoscalar-vector and isovector-vector interactions can help to reduce the symmetry energy slope,

whereas the properties of symmetric nuclear matter remain unchanged.

TABLE I: Coupling constants in the original PC-PK1 parametrization.

Coupling constant	Value	Dimension
α_S	-3.96291×10^{-4}	MeV^{-2}
β_S	8.6653×10^{-11}	MeV^{-5}
γ_S	-3.80724×10^{-17}	MeV^{-8}
δ_S	-1.09108×10^{-10}	MeV^{-4}
α_V	2.6904×10^{-4}	MeV^{-2}
γ_V	-3.64219×10^{-18}	MeV^{-8}
δ_V	-4.32619×10^{-10}	MeV^{-4}
α_{TV}	2.95018×10^{-5}	MeV^{-2}
δ_{TV}	-4.11112×10^{-10}	MeV^{-4}
γ_C	0	MeV^{-8}

In order to investigate the effect of the symmetry energy slope L on nuclear pasta phases, we generate a set of RMF-PC models with different values of L at saturation density based on the PC-PK1 parametrization. For this purpose, we introduce an additional coupling term with coefficient γ_C in Eq. (1), which corresponds to the ω - ρ coupling in the finite-range RMF models. It is well known that this term plays an important role in modifying the density dependence of the symmetry energy and affecting neutron star properties [12, 23, 45, 46, 85–88]. By simultaneously adjusting the coupling constants α_{TV} and γ_C , one can achieve a given L at saturation density ρ_0 while keeping the symmetry energy E_{sym} fixed at a density of 0.12 fm^{-3} . The resulting parameters α_{TV} and γ_C are presented in Table II. The reason for fixing E_{sym} at a density of 0.12 fm^{-3} is that the set of generated models should reproduce similar binding energies of finite nuclei with the experimental data. It has been found that the binding energy of finite nuclei is essentially determined by the symmetry energy at a density of 0.10 – 0.12 fm^{-3} , not by the one at saturation density [45, 85, 87, 91]. To examine the sensitivity of the binding energy to the fixed density ρ_{fix} of the symmetry energy, we perform a standard RMF calculation with the PC-PK1 parametrization for ^{208}Pb using different choices of ρ_{fix} . In Fig. 1, one can see that the binding energy per nucleon of ^{208}Pb remains almost unchanged with the variation of L for $\rho_{\text{fix}} = 0.12 \text{ fm}^{-3}$, whereas it deviates from the experimental value (7.87 MeV) when $\rho_{\text{fix}} = 0.11 \text{ fm}^{-3}$ or $\rho_{\text{fix}} = \rho_0$ is used. We note that the result for $L = 113 \text{ MeV}$ corresponds to the original PC-PK1 case with $\gamma_C = 0$, and therefore all three lines terminate at the same point.

We emphasize that all generated models in Table II have the same isoscalar properties and fixed symmetry energy at $\rho_B = 0.12 \text{ fm}^{-3}$, but they have different density dependence of the symmetry energy. In Fig. 2, we display the symmetry energy E_{sym} as a function of the baryon density ρ_B for the set of generated models. It is obvious

TABLE II: Parameters α_{TV} and γ_C generated from the PC-PK1 parametrization for different slope L at saturation density ρ_0 with fixed symmetry energy $E_{\text{sym}} = 27.733$ MeV at $\rho_{\text{fix}} = 0.12 \text{ fm}^{-3}$. The last line shows the symmetry energy at saturation density.

L (MeV)	40	50	60	70	80	90	100	113
α_{TV} (10^{-5} MeV^{-2})	4.0168	3.8706	3.7243	3.5780	3.4317	3.2854	3.1392	2.9502
γ_C ($10^{-18} \text{ MeV}^{-8}$)	-6.2734	-5.4131	-4.5528	-3.6924	-2.8321	-1.9718	-1.1114	0
$E_{\text{sym}}(\rho_0)$ (MeV)	31.69	32.23	32.77	33.31	33.84	34.38	34.92	35.61

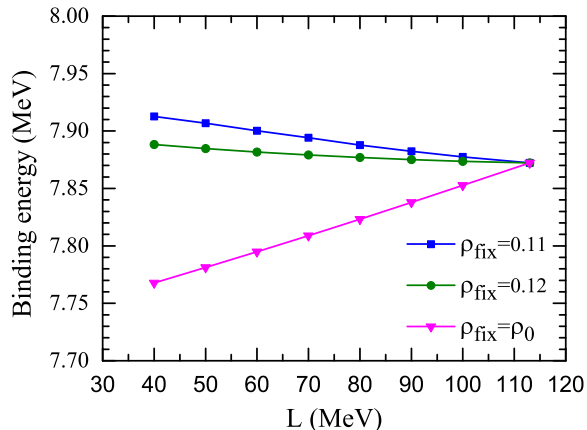


FIG. 1: Binding energy per nucleon of ^{208}Pb vs the symmetry energy slope L with different choices of ρ_{fix} based on the PC-PK1 parametrization.

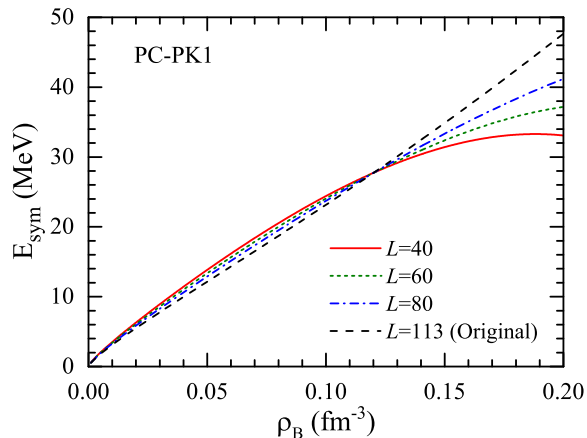


FIG. 2: Symmetry energy E_{sym} as a function of the baryon density ρ_B for the generated models with different L . The symmetry energy is fixed at a density of 0.12 fm^{-3} .

that all models have the same E_{sym} at a density of 0.12 fm^{-3} , but they have different E_{sym} at lower and higher densities due to the difference of the slope L . One can see that a smaller L corresponds to a larger (smaller) E_{sym} at lower (higher) densities. It is feasible and interesting

to use these models for studying the effect of L on pasta structures at subnuclear densities.

In the present work, we perform three-dimensional calculations in a large cubic cell with the periodic boundary condition. Considering the balance between desired accuracy and computational time, we use the cell size of 60 fm with 64 grid points in each direction. Such choices are generally large enough for obtaining convergent results in three-dimensional calculations of nuclear pasta [30, 35]. It was reported in Ref. [35] that changing the box size from 24 fm to 48 fm in the Skyrme Hartree-Fock calculation would not significantly change the total energies of the ground state. In our calculations, enlarging the number of grid points from 64 to 128 leads to a energy difference within a few keV, which is negligible for determining the pasta configuration. The computational time in three-dimensional calculations is estimated to scale as n^3 , where n is the number of grid points in each direction. Therefore, the calculation with a larger n is much more time-consuming. Using the cell size of 60 fm with $n = 64$, the grid spacing is 0.9375 fm, which is a reasonable value for three-dimensional calculations of nuclear pasta [30, 35]. At a typical density of $\rho_B = 0.05 \text{ fm}^{-3}$, there are about 10800 nucleons in a cubic cell with the size of 60 fm, where several periods of pasta structures can be formed (see Figs. 3, 5, and 6 below).

IV. RESULTS AND DISCUSSION

In this section, we present the results of three-dimensional calculations for nonuniform matter at subnuclear densities. We explore the pasta structures for both cold stellar matter with a fixed proton fraction and neutron-star matter in β equilibrium. The influence of nuclear symmetry energy is examined by using the generated models from the PC-PK1 parametrization.

A. Pasta structures with a fixed proton fraction

We first present and compare the pasta structures for fixed proton fraction by using two limit RMF-PC models in Table II, namely the ones with $L = 40$ and 113 MeV. In symmetric nuclear matter ($Y_p = 0.5$), these two models provide almost the same features of pasta struc-

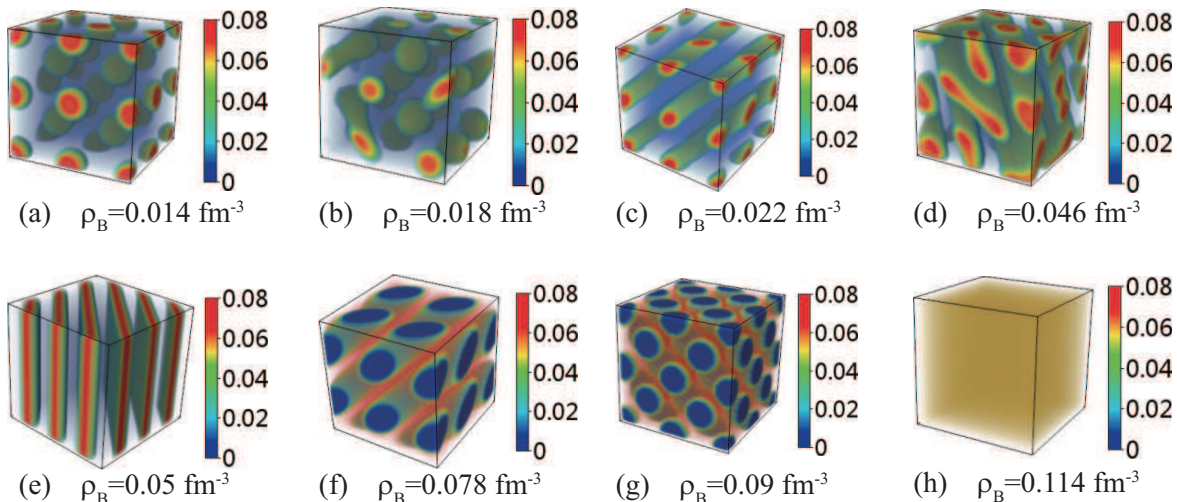


FIG. 3: Proton density distributions in pasta phases for $Y_p = 0.5$ obtained using the RMF-PC model with $L = 40$ MeV.

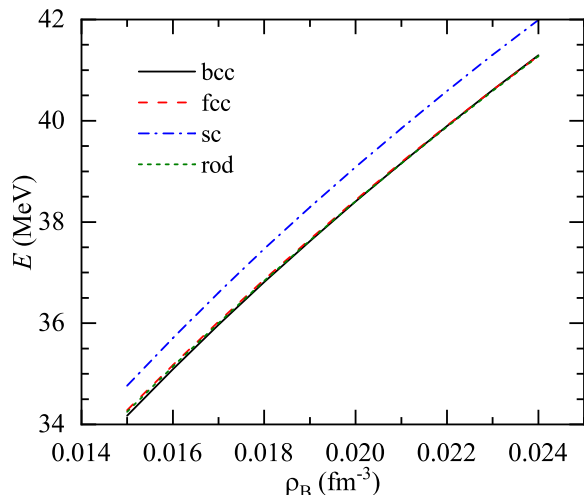


FIG. 4: Energy per nucleon E for different configurations observed around the transition from droplets to rods.

tures. In Fig. 3, we show the proton density distributions of nonuniform matter for $Y_p = 0.5$ in a cubic cell with a length of 60 fm. The results are obtained from the three-dimensional Thomas-Fermi calculations by using the RMF-PC model with $L = 40$ MeV. At a low density of $\rho_B = 0.014 \text{ fm}^{-3}$, the matter forms a crystalline structure of droplets. As the density ρ_B increases, typical pasta phases like rods, slabs, tubes, and bubbles are observed before the transition to uniform matter. In addition, some intermediate structures around the shape transition are also observed [see Fig. 3(b) and 3(d)], which make the transition between different shapes more smooth. In our calculations, the ground state at low densities is a body-centered cubic (bcc) lattice of droplets, whereas a face-centered cubic (fcc) lattice may appear as

a metastable state. This is consistent with the previous studies in Refs. [24, 76], but inconsistent with the results in Refs. [13, 30] where the fcc lattice is energetically more favorable than the bcc one. In practical calculations, the final configurations are somewhat influenced by the initial density distributions. When different initial configurations are used, some metastable states may arrive after the convergence is achieved. In Fig. 4, we compare the energy per nucleon E among different configurations observed around the transition from droplets to rods. It is found that a simple cubic (sc) lattice of droplets emerges as a metastable state at low densities, whose energy is obviously larger than that of the bcc lattice. On the other hand, the energy of an fcc lattice is only slightly higher than that in the bcc case, while their energy difference decreases as the density increases. At the density $\rho_B > 0.02 \text{ fm}^{-3}$, the rod phase becomes the ground state with the lowest energy, but its energy per nucleon E is only a few keV lower than that of the bcc lattice. In Fig. 3(g), an fcc lattice of bubbles is observed before the transition to uniform matter, which is consistent with the results in Refs. [13, 30].

To explore the influence of symmetry energy and its slope, we compare the pasta structures obtained using the models with $L = 40$ and 113 MeV for lower values of Y_p , where the isovector part is expected to play a crucial role. In Figs. 5 and 6, we display the proton density distributions in typical pasta phases for $Y_p = 0.3$ and 0.05, respectively. It is found that the pasta structures obtained with $L = 40$ MeV (left panels) and $L = 113$ MeV (right panels) show similar features in the case of $Y_p = 0.3$, but significant differences are observed for a low value of $Y_p = 0.05$. In Fig. 6, one can see that the proton densities at the center of nuclear pastas obtained with $L = 40$ MeV is relatively larger than that of $L = 113$ MeV. Furthermore, at a density of $\rho_B = 0.076 \text{ fm}^{-3}$, the matter forms a crystalline structure of bubbles with

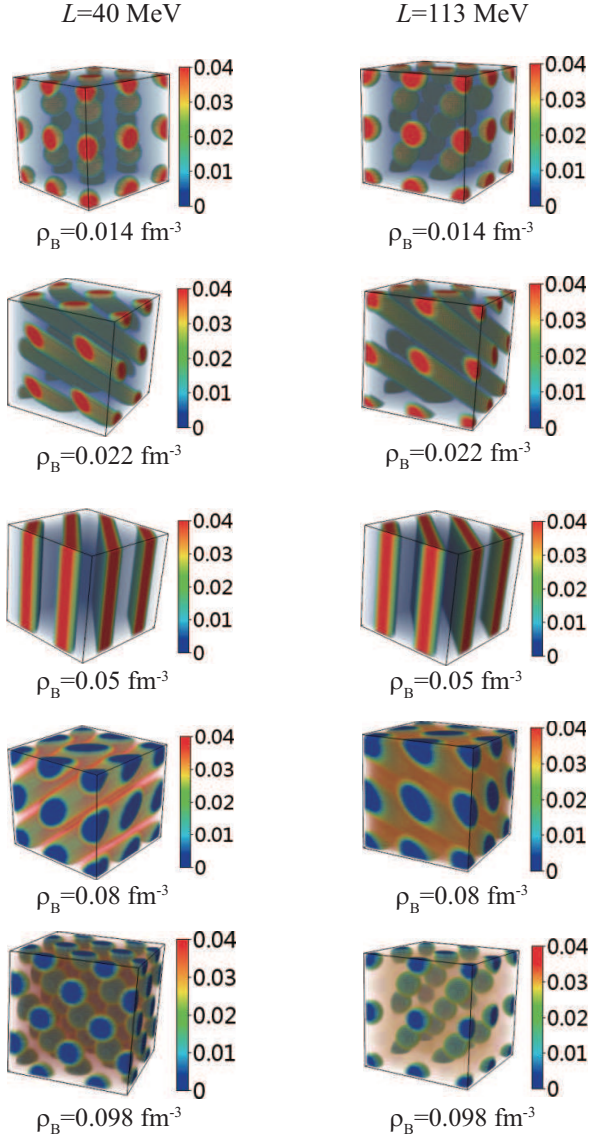


FIG. 5: Proton density distributions in typical pasta phases at a fixed proton fraction of $Y_p = 0.3$. The results obtained with $L = 40$ MeV (left panels) are compared to those with $L = 113$ MeV (right panels).

$L = 40$ MeV, but it is already in uniform phase with $L = 113$ MeV. The differences of pasta properties between $L = 40$ and 113 MeV can be seen more clearly in Fig. 7, where the density profiles in droplet configurations for different Y_p are displayed along a line passing through the center of the droplets. In the top panel with $Y_p = 0.5$, there is no visible difference in the density distributions between the two models. With decreasing Y_p , one can see that the model with $L = 40$ MeV results in larger neutron densities at the center of the droplet compared to that with $L = 113$ MeV, and this trend is more pronounced for lower values of Y_p . Meanwhile, the proton densities at the center of the droplets with

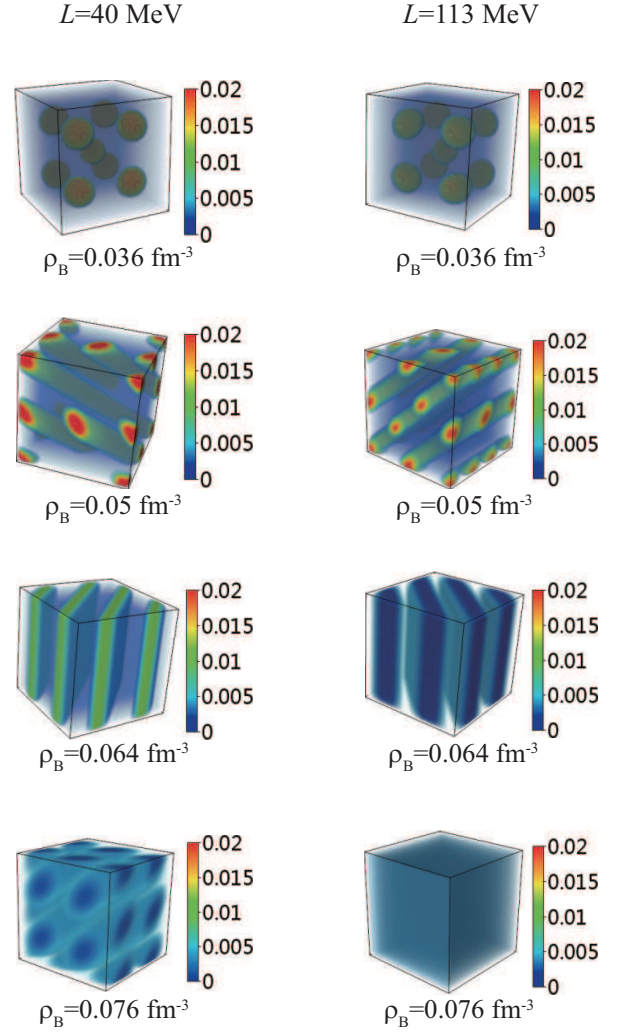


FIG. 6: Proton density distributions in typical pasta phases at a fixed proton fraction of $Y_p = 0.05$. The results obtained with $L = 40$ MeV (left panels) are compared to those with $L = 113$ MeV (right panels).

$L = 40$ MeV are only slightly higher than those with $L = 113$ MeV. This behavior can be understood from the density dependence of the symmetry energy E_{sym} shown in Fig. 2. With a smaller slope $L = 40$ MeV, E_{sym} is relatively small at higher densities ($\rho_B > 0.12 \text{ fm}^{-3}$), which leads to larger neutron densities at the center of the droplet. Similar differences between $L = 40$ and 113 MeV are also observed in other pasta configurations. On the other hand, we can see that dripped neutrons exist outside the droplets for small values of $Y_p = 0.1$ and 0.05, whereas all nucleons participate in forming nuclear clusters for $Y_p = 0.3$ and 0.5. Generally, a free neutron gas may appear for $Y_p < 0.3$ and its density increases with decreasing Y_p .

In Fig. 8, we show the energy per nucleon E as a function of the baryon density ρ_B for $Y_p = 0.5, 0.3, 0.1,$ and 0.05. For comparison, the results of uniform matter

are displayed by dashed lines, which are obviously higher than those of pasta phases at lower densities. The results obtained with $L = 40$ MeV (left panels) are compared to those with $L = 113$ MeV (right panels). One can see that the behaviors of E are very similar between these two models for larger values of $Y_p = 0.5$ and 0.3 , whereas significant differences are observed for $Y_p = 0.1$ and 0.05 . The model with $L = 40$ MeV predicts relatively large E and late transition to uniform matter compared to that with $L = 113$ MeV. This is because E_{sym} in the model with $L = 40$ MeV is larger than that with $L = 113$ MeV at low densities (see Fig. 2). It is seen that the transition from pasta phase to uniform matter occurs at lower densities for smaller values of Y_p , and some pasta shapes like the bubble configuration could not appear before the transition to uniform matter in the case of $Y_p = 0.05$.

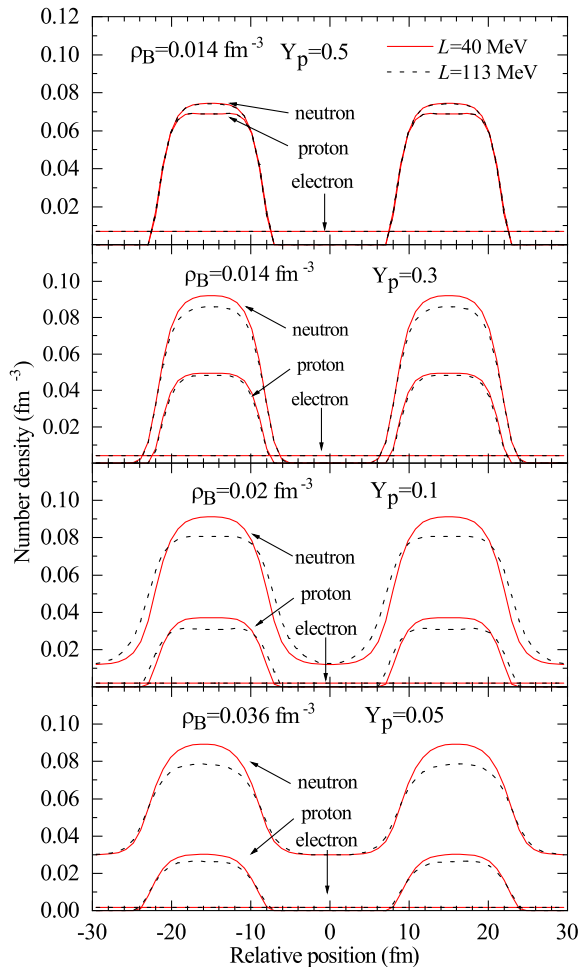


FIG. 7: Density distributions of protons, neutrons, and electrons along a line passing through the center of the droplets. The results obtained with $L = 40$ MeV (solid lines) are compared to those with $L = 113$ MeV (dashed lines).

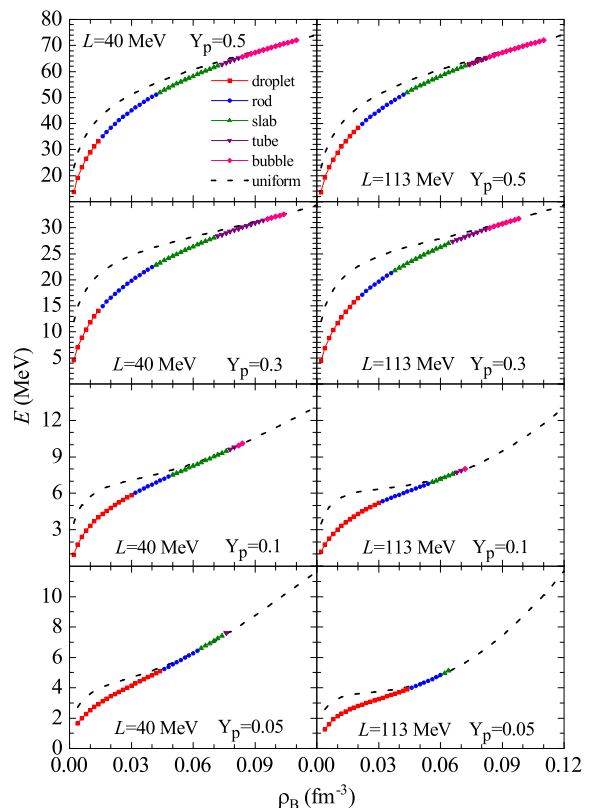


FIG. 8: Energy per nucleon E as a function of the baryon density ρ_B for $Y_p = 0.5, 0.3, 0.1,$ and 0.05 using the models with $L = 40$ MeV (left panels) and $L = 113$ MeV (right panels). For comparison, the results of uniform matter are also displayed by dashed lines.

B. Inner crust of neutron stars

To describe nonuniform matter in the inner crust of neutron stars, we perform fully three-dimensional calculations in a cubic box with periodic boundary conditions, where the conditions of β equilibrium and charge neutrality are satisfied. We carry out the calculations using the models with $L = 40$ and 113 MeV, so as to examine the influence of the symmetry energy slop L . The matter in neutron-star crusts contains protons, neutrons, and electrons, where the proton fraction Y_p is determined by the β equilibrium condition and its value is sensitive to the behavior of the symmetry energy. In Fig. 9, we display the proton fraction Y_p of nonuniform matter in neutron-star crusts as a function of the baryon density ρ_B using the models with $L = 40$ and 113 MeV, where the results of uniform matter are also shown for comparison. It is found that both models predict rather small values of Y_p in the density region of $0.02 < \rho_B < 0.12 \text{ fm}^{-3}$, where nonspherical pasta structures are expected to appear. However, only spherical droplets are observed in our calculations before the crust-core transition which occurs at $\rho_B \simeq 0.072 \text{ fm}^{-3}$ with $L = 40$ MeV and at

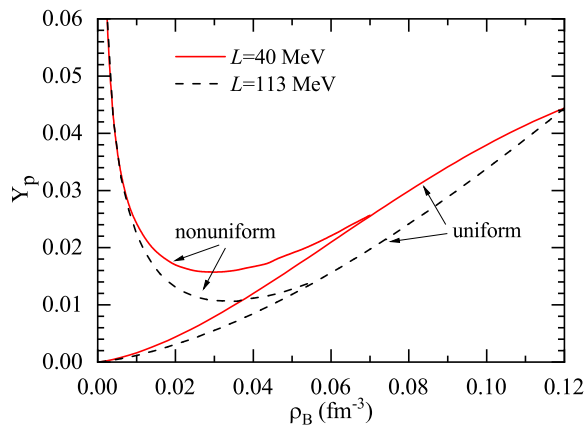


FIG. 9: Proton fractions as a function of the baryon density in neutron-star matter with nonuniform and uniform distributions.

$\rho_B \simeq 0.057 \text{ fm}^{-3}$ with $L = 113 \text{ MeV}$. Due to smaller values of Y_p obtained in β equilibrium, it is unlikely to form nonspherical pasta in neutron-star crusts, and meanwhile the transition to uniform matter occurs at lower densities. This is in contrast to the results with a fixed Y_p shown in the previous subsection. One can see that at low densities, Y_p of nonuniform matter is significantly larger than that of uniform matter. This is because the formation of nuclear clusters can largely reduce the chemical potential of protons, which leads to an enhancement of Y_p in nonuniform matter. Comparing the results between $L = 40$ and 113 MeV , we see that a smaller L corresponds to a larger Y_p in both nonuniform and uniform cases. This correlation can be understood from the density dependence of the symmetry energy E_{sym} shown in Fig. 2. At low densities ($\rho_B < 0.12 \text{ fm}^{-3}$), the model with $L = 40 \text{ MeV}$ has larger E_{sym} than that with $L = 113 \text{ MeV}$, and as a result, it favors to contain more protons in the system.

In Fig. 10, we plot the density distributions of protons, neutrons, and electrons in β equilibrium along a line passing through the center of the droplets. At a low density of $\rho_B = 0.01 \text{ fm}^{-3}$ (top panel), nuclear clusters are formed in a dripped neutron gas with large space between the clusters. At $\rho_B = 0.041 \text{ fm}^{-3}$ (bottom panel), the distance between droplets becomes relatively small and the dripped neutrons are significantly enhanced. One can see that there are clear differences between the results of $L = 40$ and 113 MeV . The model with $L = 40 \text{ MeV}$ yields larger neutron and proton densities at the center of droplets compared to those with $L = 113 \text{ MeV}$, and the difference is more pronounced for neutrons. This effect is caused by different density dependence of the symmetry energy E_{sym} (see Fig. 2), where a smaller E_{sym} at $\rho_B > 0.12 \text{ fm}^{-3}$ with $L = 40 \text{ MeV}$ leads to larger neutron densities inside nuclear clusters. In Fig. 11, we display the energy per nucleon E as a function of the

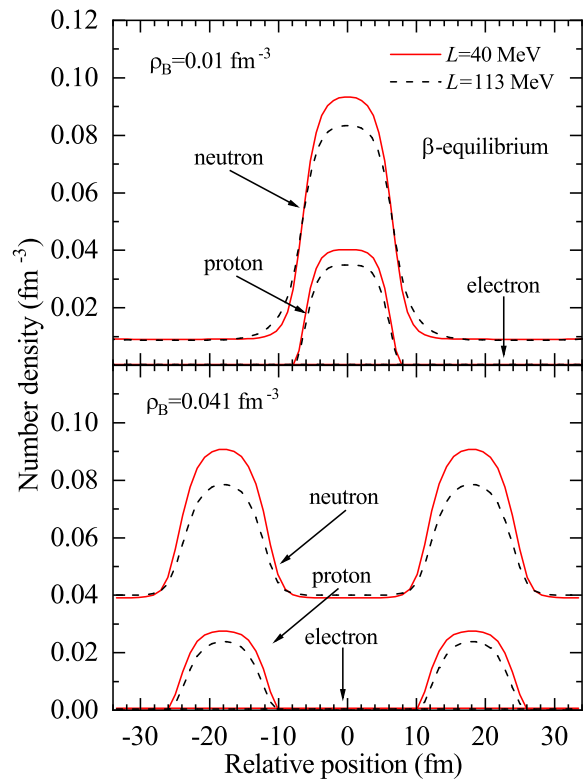


FIG. 10: Density distributions of protons, neutrons, and electrons in β equilibrium along a line passing through the center of the droplets. The results obtained with $L = 40 \text{ MeV}$ are compared to those of $L = 113 \text{ MeV}$.

baryon density ρ_B for neutron-star matter in β equilibrium. Compared to the case with fixed Y_p in Fig. 8, the reduction of E in nonuniform matter is less pronounced. This is because Y_p in β equilibrium is rather small (see Fig. 9), that only small fraction of nucleons can form clusters which do not affect the total energy very much. It is shown that E obtained with $L = 40 \text{ MeV}$ is higher than that with $L = 113 \text{ MeV}$, since the model with $L = 40 \text{ MeV}$ has larger symmetry energy E_{sym} at low densities.

To study the correlation between the symmetry energy slope L and the crust-core transition, we perform calculations for nonuniform matter in β equilibrium by employing the set of generated models given in Table II. We display in Fig. 12 the crust-core transition density $\rho_{B,t}$ and proton fraction at the transition point $Y_{p,t}$ as a function of L using the generated models based on the PC-PK1 parametrization. It is shown that both $\rho_{B,t}$ and $Y_{p,t}$ decrease with increasing L . These correlations are consistent with those reported in Refs. [12, 25, 44, 48–50]. In the present work, we obtain $\rho_{B,t} = 0.072 \text{ fm}^{-3}$ for $L = 40 \text{ MeV}$, and it decreases to 0.057 fm^{-3} for $L = 113 \text{ MeV}$. The correlation between $\rho_{B,t}$ and L can be understood from an analysis in the liquid-drop model [44], where the energy-density curvature of pure neutron matter at saturation density is approximately proportional

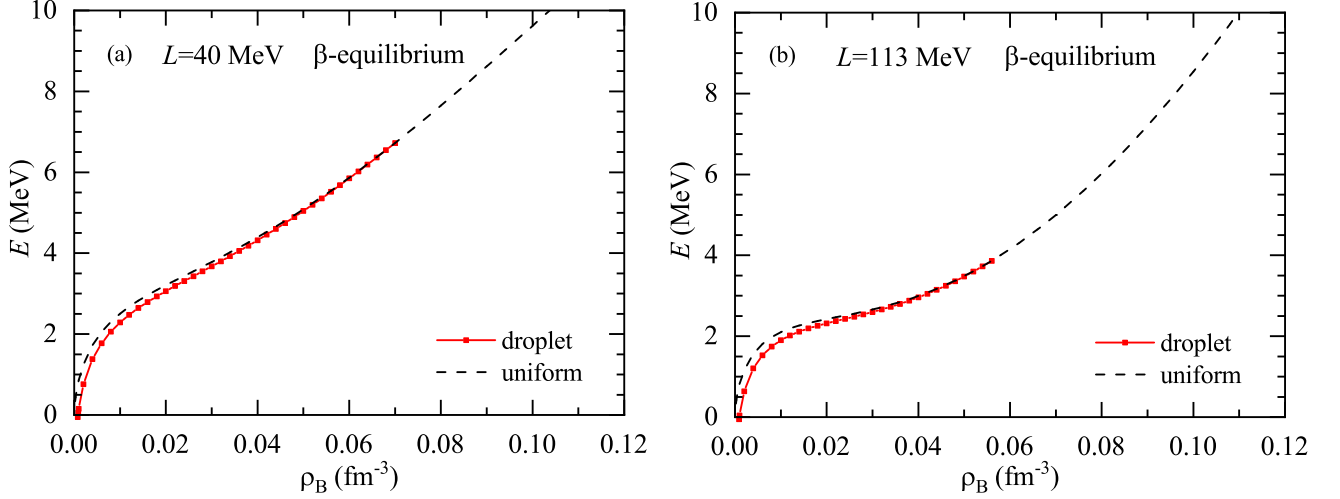


FIG. 11: Energy per nucleon E as a function of the baryon density ρ_B using the models with $L = 40$ MeV (a) and $L = 113$ MeV (b). For comparison, the results of uniform matter are also displayed by dashed lines.

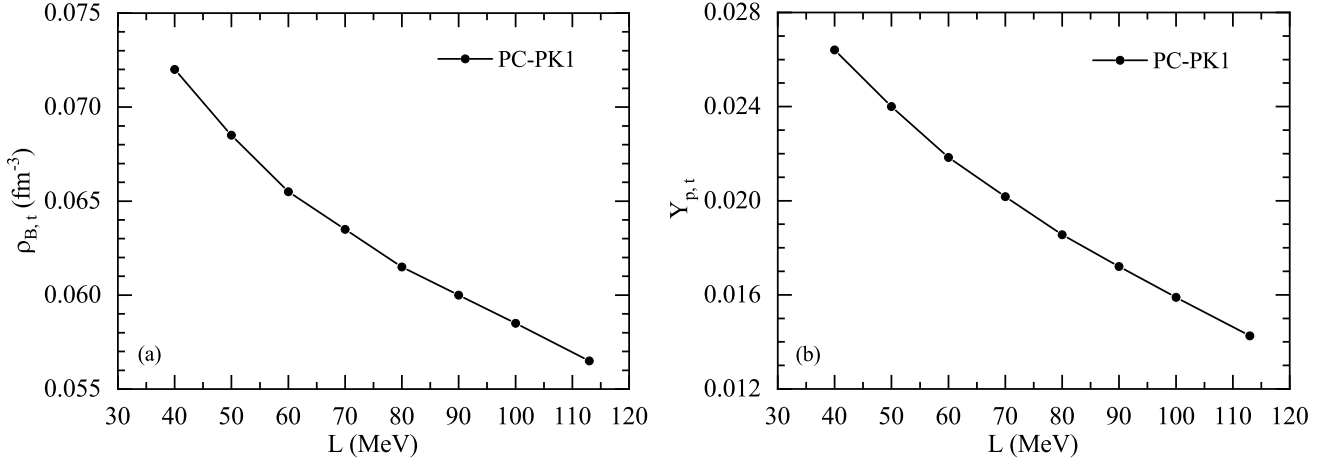


FIG. 12: Crust-core transition density $\rho_{B,t}$ (a) and proton fraction at the transition point $Y_{p,t}$ (b) as a function of the symmetry energy slope L using the generated models based on the PC-PK1 parametrization.

to L . The crust-core transition occurs when the energy-density curvature becomes negative, i.e., spinodal instability. This implies that a larger L requires a lower $\rho_{B,t}$ for reaching the negative curvature region. On the other hand, the decrease of $Y_{p,t}$ is related to the density dependence of E_{sym} . The model with a larger L has a smaller E_{sym} at $\rho_B < 0.12 \text{ fm}^{-3}$, so it results in a smaller $Y_{p,t}$ at the transition point. It is noteworthy that the crust-core transition depends on both nuclear interaction and description of nonuniform matter.

C. Properties of neutron stars

The properties of neutron stars, such as mass-radius relations and tidal deformabilities, can be obtained by solving the Tolman-Oppenheimer-Volkoff (TOV) equation using the EOS over a wide range of densities. Generally, the EOS is composed of three segments: the outer crust, the inner crust, and the liquid core. In the present work, we focus on nonuniform structure of the inner crust. It is interesting to explore the possible influence from the inner crust on various properties of neutron stars. In practical calculations, we adopt the Baym-Pethick-Sutherland (BPS) EOS [92] for the outer crust below the neutron drip density, while the EOS obtained from our three-dimensional calculations is adopted for

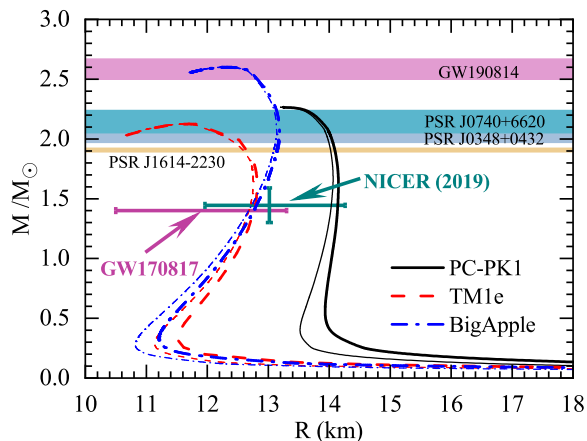


FIG. 13: Mass-radius relations of neutron stars by using different combinations of the core and crust segments. The results using the inner crust EOS with $L=40$ and 113 MeV are shown by thick and thin lines, respectively. The colored horizontal bars indicate the mass measurements of PSR J1614–2230 [95–97], PSR J0348+0432 [98], and PSR J0740+6620 [99], while the mass constraint from GW190814 [67] is shown in pink color. The constraints from NICER [69] and GW170817 [59] are also indicated.

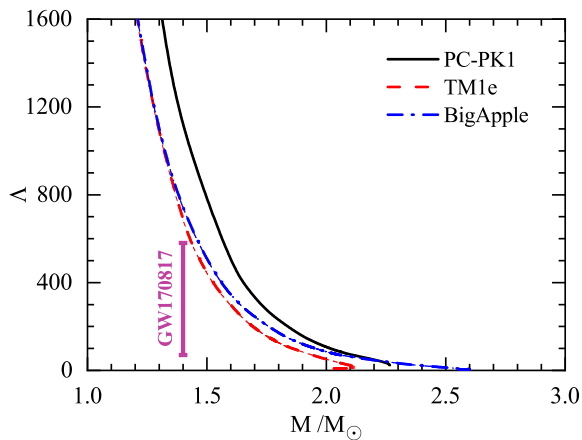


FIG. 14: Dimensionless tidal deformability Λ as a function of the neutron-star mass M . The vertical line represents the constraints on $\Lambda_{1.4}$ from the analysis of GW170817 [59].

the inner crust. It is known that the mass-radius relations of neutron stars are dominantly determined by the core EOS at high densities, where large uncertainties exist among different models. Considering observational constraints on neutron-star masses and radii, we employ several core EOSs, namely PC-PK1 [90], TM1e [93], and BigApple [94], which are matched to the inner crust segments around the transition density. The PC-PK1 parametrization of the RMF-PC model used in our calculations of nonuniform matter has a large symmetry energy slope $L = 113$ MeV, which predicts rather large radii

and tidal deformabilities of neutron stars as reported in Ref. [90]. Furthermore, the contribution from γ_V relevant term in Eq. (1) may result in negative pressures at high densities, which leads to the difficulty of reaching the maximum mass of neutron stars. The TM1e and BigApple parametrizations in the RMF approach have relatively small slope parameter $L \simeq 40$ MeV, which are more consistent with current constraints from astrophysical observations. The TM1e parametrization has been successfully used to construct the EOS for numerical simulations of core-collapse supernovae [93]. The BigApple parametrization has been proposed to account for a $2.6M_\odot$ compact object observed in GW190814 [94]. We note that all of the models can provide satisfactory descriptions of finite nuclei, and meanwhile they can satisfy the $2M_\odot$ constraint for neutron stars.

To examine the influence of the inner crust, we adopt the EOS of nonuniform matter based on the RMF-PC models with $L = 40$ and 113 MeV, as described in the previous section. In Fig. 13, we display the resulting mass-radius relations of neutron stars by using different combinations of the core and crust segments. The results using the inner crust EOS with $L = 40$ and 113 MeV are shown by thick and thin lines, respectively. It is found that massive neutron stars are insensitive to the inner crust EOS, while visible differences are observed in low-mass neutron stars. For the same core EOS, the radii of neutron stars obtained using the inner crust EOS with $L = 40$ MeV are slightly larger than that with $L = 113$ MeV. On the other hand, the differences caused by the core EOS are much more pronounced. In the case with the PC-PK1 core EOS, its large symmetry energy slope $L = 113$ MeV results in the radius of a canonical $1.4M_\odot$ neutron star, $R_{1.4} \sim 14$ km, which is disfavored by the constraints from NICER [69] and GW170817 [59]. In contrast, the radii of a $1.4M_\odot$ neutron star obtained using the TM1e and BigApple core EOSs are more consistent with current constraints, which are related to their small slope parameters. One can see that the mass-radius curves in the TM1e and BigApple cases go past the maximum mass star configuration, where the maximum masses predicted by TM1e and BigApple are about $2.12M_\odot$ and $2.60M_\odot$, respectively. It is shown that the maximum neutron-star masses can be significantly affected by the core EOS at high densities, while the influence of the inner crust EOS is almost invisible. In all cases, the results are compatible with the mass measurements of PSR J1614–2230 [95–97], PSR J0348+0432 [98], and PSR J0740+6620 [99], but only BigApple core EOS can support a $2.6M_\odot$ neutron star.

The dimensionless tidal deformability of a neutron star is calculated from

$$\Lambda = \frac{2}{3}k_2 (R/M)^5, \quad (11)$$

where k_2 is the tidal Love number which is computed together with the TOV equation [47]. In Fig. 14, we display the dimensionless tidal deformability Λ as a function of

the neutron-star mass M . The results using the inner crust EOS with $L = 40$ and 113 MeV are shown by thick and thin lines, respectively. The influence caused by different crust EOS is small, but the core EOS can significantly alter the tidal deformability Λ . The results of Λ using the PC-PK1 core EOS are much larger than the constraints from GW170817 [59] due to its large symmetry energy slope. The TM1e and BigApple core EOSs predict relatively small tidal deformabilities which are more consistent with the constraints from GW170817 [58, 59, 94].

V. CONCLUSIONS

In the present work, we have studied the properties of nuclear pasta phases, which may occur not only in the inner crust of neutron stars but also in stellar matter with a relatively large proton fraction. We have performed fully three-dimensional Thomas-Fermi calculations in a cubic box with periodic boundary conditions. The calculations were carried out for both cold stellar matter with a fixed proton fraction and neutron-star matter in β equilibrium. For the nuclear interaction, we have employed the RMF-PC approach with the PC-PK1 parametrization, which could provide a good description of ground-state properties for the nuclei all over the nuclear chart. In order to examine the influence of nuclear symmetry energy and its slope parameter L , we have generated a set of models with different L at saturation density based on the PC-PK1 parametrization by introducing an additional coupling term between the isoscalar-vector and isovector-vector interactions. All generated models have the same isoscalar properties and fixed symmetry energy E_{sym} at $\rho_B = 0.12 \text{ fm}^{-3}$, which ensure to provide similar binding energies of finite nuclei with the experimental data, but they have different density dependences of E_{sym} that may play a crucial role in determining nonuniform structures in the neutron-rich matter.

We have investigated the pasta structures in nuclear matter with a fixed proton fraction Y_p by using two limit models with $L = 40$ and 113 MeV. It was found that these two models provide similar features of pasta structures for $0.3 \leq Y_p \leq 0.5$, but significant differences could

be observed in the low Y_p region, where the symmetry energy is expected to play an important role. Generally, the ground state of nonuniform matter at low densities is a bcc lattice of droplets, while nonspherical pasta phases may appear at the density $\rho_B > 0.02 \text{ fm}^{-3}$. The onset density of nonspherical shapes increases as the proton fraction Y_p decreases. In our three-dimensional calculations, typical geometric shapes like droplets, rods, slabs, tubes, and bubbles were observed before the transition to uniform matter. In addition, some intermediate structures around the shape transition were also observed, which would make the transition between different shapes more smooth.

For neutron-star matter in β equilibrium, we found only spherical droplets were formed before the transition to uniform matter using the models with $L = 40$ and 113 MeV. The values of Y_p obtained in β equilibrium are very small, which lead to an early onset of uniform matter. The crust-core transition occurs at $\rho_B \simeq 0.072 \text{ fm}^{-3}$ with $L = 40$ MeV and at $\rho_B \simeq 0.057 \text{ fm}^{-3}$ with $L = 113$ MeV. We studied the correlations between the symmetry energy slope L and the crust-core transition by employing the set of generated models. It was seen that both the baryon density and the proton fraction at the crust-core transition decrease with increasing L . The resulting EOSs of the inner crust using the models with $L = 40$ and 113 MeV were applied to study the properties of neutron stars. It was shown that massive neutron stars are insensitive to the inner crust EOS, while visible differences could be observed in the radii of low-mass neutron stars. We emphasize that although nonuniform structures in the inner crust have less influence on the bulk properties of neutron stars, they may be important for interpreting cooling observations. In addition, the properties of pasta phases in supernova matter would affect the neutrino signal, which need further investigation.

Acknowledgement

This work was supported in part by the National Natural Science Foundation of China (Grants No. 11675083 and No. 11775119)

-
- [1] J. M. Lattimer and M. Prakash, *Science* **304**, 536 (2004).
 - [2] A. Burrows, E. Livne, L. Dessart, C. D. Ott, and J. Murphy, *Astrophys. J.* **640**, 878 (2006).
 - [3] K. Sumiyoshi, S. Yamada, H. Suzuki, and S. Chiba, *Phys. Rev. Lett.* **97**, 091101 (2006).
 - [4] M. Oertel, M. Hempel, T. Klähn, and S. Typel, *Rev. Mod. Phys.* **89**, 015007 (2017).
 - [5] H. Shen, H. Toki, K. Oyamatsu, and K. Sumiyoshi, *Astrophys. J. Suppl.* **197**, 20 (2011).
 - [6] N. Chamel and P. Haensel, *Living Rev. Relativ.* **11**, 10 (2008).
 - [7] H. Heiselberg and M. Hjorth-Jensen, *Phys. Rep.* **328**, 237 (2000).
 - [8] F. Weber, *Prog. Part. Nucl. Phys.* **54**, 193 (2005).
 - [9] D. G. Ravenhall, C. J. Pethick, and J. R. Wilson, *Phys. Rev. Lett.* **50**, 2066 (1983).
 - [10] A. W. Steiner, *Phys. Rev. C* **77**, 035805 (2008).
 - [11] F. Grill, C. Providência, and S. S. Avancini, *Phys. Rev. C* **85**, 055808 (2012).
 - [12] S. S. Bao and H. Shen, *Phys. Rev. C* **91**, 015807 (2015).
 - [13] M. Okamoto, T. Maruyama, K. Yabana, and T. Tatsumi, *Phys. Rev. C* **88**, 025801 (2013).
 - [14] F. J. Fattoyev, C. J. Horowitz, and B. Schuetrumpf, *Phys. Rev. C* **95**, 055804 (2017).

- [15] H. Pais, S. Chiacchiera, and C. Providência, *Phys. Rev. C* **91**, 055801 (2015).
- [16] A. Roggero, J. Margueron, L. F. Roberts, and S. Reddy, *Phys. Rev. C* **97**, 045804 (2018).
- [17] C. J. Horowitz, D. K. Berry, M. E. Caplan, T. Fischer, Z. Lin, W. G. Newton, E. O'Connor, and L. F. Roberts, arXiv:1611.10226.
- [18] B. P. Abbott *et al.* (LIGO Scientific Collaboration and Virgo Collaboration), *Phys. Rev. D* **96**, 122006 (2017).
- [19] C. J. Pethick, Z. W. Zhang, and D. N. Kobyakov, *Phys. Rev. C* **101**, 055802 (2020).
- [20] C. J. Pethick, *Acta Phys. Pol. B* **50**, 2145 (2019).
- [21] M. E. Caplan, A. S. Schneider, and C. J. Horowitz, *Phys. Rev. Lett.* **121**, 132701 (2018).
- [22] G. Watanabe, K. Iida, and K. Sato, *Nucl. Phys. A* **676**, 455 (2000).
- [23] S. S. Bao and H. Shen, *Phys. Rev. C* **89**, 045807 (2014).
- [24] K. Oyamatsu, *Nucl. Phys. A* **561**, 431 (1993).
- [25] K. Oyamatsu and K. Iida, *Phys. Rev. C* **75**, 015801 (2007).
- [26] S. S. Avancini, D. P. Menezes, M. D. Alloy, J. R. Marinelli, M. M. W. Moraes, and C. Providência, *Phys. Rev. C* **78**, 015802 (2008).
- [27] S. S. Avancini, S. Chiacchiera, D. P. Menezes, and C. Providência, *Phys. Rev. C* **82**, 055807 (2010); **85**, 059904(E) (2012).
- [28] F. Grill, H. Pais, C. Providência, I. Vidaña, and S. S. Avancini, *Phys. Rev. C* **90**, 045803 (2014).
- [29] R. D. Williams and S. E. Koonin, *Nucl. Phys. A* **435**, 844 (1985).
- [30] M. Okamoto, T. Maruyama, K. Yabana, and T. Tatsumi, *Phys. Lett. B* **713**, 284 (2012).
- [31] P. Magierski and P.-H. Heenen, *Phys. Rev. C* **65**, 045804 (2002).
- [32] W. G. Newton and J. R. Stone, *Phys. Rev. C* **79**, 055801 (2009).
- [33] H. Pais and J. R. Stone, *Phys. Rev. Lett.* **109**, 151101 (2012).
- [34] B. Schuetrumpf, M. A. Klatt, K. Iida, J. A. Maruhn, K. Mecke, and P.-G. Reinhard, *Phys. Rev. C* **87**, 055805 (2013).
- [35] I. Sagert, G. I. Fann, F. J. Fattoyev, S. Postnikov, and C. J. Horowitz, *Phys. Rev. C* **93**, 055801 (2016).
- [36] M. E. Caplan and C. J. Horowitz, *Rev. Mod. Phys.* **89**, 041002 (2017).
- [37] T. Maruyama, K. Niita, K. Oyamatsu, T. Maruyama, S. Chiba, and A. Iwamoto, *Phys. Rev. C* **57**, 655 (1998).
- [38] H. Sonoda, G. Watanabe, K. Sato, K. Yasuoka, and T. Ebisuzaki, *Phys. Rev. C* **77**, 035806 (2008); **81**, 049902(E) (2010).
- [39] G. Watanabe, H. Sonoda, T. Maruyama, K. Sato, K. Yasuoka, and T. Ebisuzaki, *Phys. Rev. Lett.* **103**, 121101 (2009).
- [40] A. S. Schneider, C. J. Horowitz, J. Hughto, and D. K. Berry, *Phys. Rev. C* **88**, 065807 (2013).
- [41] A. S. Schneider, D. K. Berry, C. M. Briggs, M. E. Caplan, and C. J. Horowitz, *Phys. Rev. C* **90**, 055805 (2014).
- [42] B. A. Li, L. W. Chen, and C. M. Ko, *Phys. Rep.* **464**, 113 (2008).
- [43] M. Baldo and G. F. Burgio, *Prog. Part. Nucl. Phys.* **91**, 203 (2016).
- [44] C. Ducoin, J. Margueron, and C. Providência, *Europhys. Lett.* **91**, 32001 (2010).
- [45] R. Cavagnoli, D. P. Menezes, and C. Providência, *Phys. Rev. C* **84**, 065810 (2011).
- [46] C. Providência and A. Rabhi, *Phys. Rev. C* **87**, 055801 (2013).
- [47] F. Ji, J. N. Hu, S. S. Bao, and H. Shen, *Phys. Rev. C* **100**, 045801 (2019).
- [48] C. Ducoin, C. Providência, A. M. Santos, L. Brito, and Ph. Chomaz, *Phys. Rev. C* **78**, 055801 (2008).
- [49] H. Pais, A. Sulaksono, B. K. Agrawal, and C. Providência, *Phys. Rev. C* **93**, 045802 (2016).
- [50] H. Pais and C. Providência, *Phys. Rev. C* **94**, 015808 (2016).
- [51] I. Tews, J. M. Lattimer, A. Ohnishi, and E. E. Kolomeitsev, *Astrophys. J.* **848**, 105 (2017).
- [52] K. Hebeler, J. M. Lattimer, C. J. Pethick, and A. Schwenk, *Astrophys. J.* **773**, 11 (2013).
- [53] J. M. Lattimer and A. W. Steiner, *Eur. Phys. J. A* **50**, 40 (2014).
- [54] G. Hagen, A. Ekström, C. Forssén, G. R. Jansen, W. Nazarewicz, T. Papenbrock, K. A. Wendt, S. Bacca, N. Barnea, B. Carlsson, C. Drischler, K. Hebeler, M. Hjorth-Jensen, M. Miorelli, G. Orlandini, A. Schwenk, and J. Simonis, *Nat. Phys.* **12**, 186 (2015).
- [55] X. Roca-Maza, X. Viñas, M. Centelles, B. K. Agrawal, G. Colò, N. Paar, J. Piekarewicz, and D. Vretenar, *Phys. Rev. C* **92**, 064304 (2015).
- [56] J. Birkhan, M. Miorelli, S. Bacca, S. Bassauer, C. A. Bertulani, G. Hagen, H. Matsubara, P. von Neumann-Cosel, T. Papenbrock, N. Pietralla, V. Yu. Ponomarev, A. Richter, A. Schwenk, and A. Tamii, *Phys. Rev. Lett.* **118**, 252501 (2017).
- [57] P. Danielewicz, P. Singh, and J. Lee, *Nucl. Phys. A* **958**, 147 (2017).
- [58] B. P. Abbott *et al.* (LIGO Scientific Collaboration and Virgo Collaboration), *Phys. Rev. Lett.* **119**, 161101 (2017).
- [59] B. P. Abbott *et al.* (LIGO Scientific Collaboration and Virgo Collaboration), *Phys. Rev. Lett.* **121**, 161101 (2018).
- [60] B. P. Abbott *et al.* (LIGO Scientific Collaboration and Virgo Collaboration), *Phys. Rev. X* **9**, 011001 (2019).
- [61] I. Tews, J. Margueron, and S. Reddy, *Phys. Rev. C* **98**, 045804 (2018).
- [62] S. De, D. Finstad, J. M. Lattimer, D. A. Brown, E. Berger, and C. M. Biwer, *Phys. Rev. Lett.* **121**, 091102 (2018).
- [63] F. J. Fattoyev, J. Piekarewicz, and C. J. Horowitz, *Phys. Rev. Lett.* **120**, 172702 (2018).
- [64] T. Malik, N. Alam, M. Fortin, C. Providência, B. K. Agrawal, T. K. Jha, B. Kumar, and S. K. Patra, *Phys. Rev. C* **98**, 035804 (2018).
- [65] Z. Y. Zhu, E. P. Zhou, and A. Li, *Astrophys. J.* **862**, 98 (2018).
- [66] B. P. Abbott *et al.* (LIGO Scientific Collaboration and Virgo Collaboration), *Astrophys. J. Lett.* **892**, L3 (2020).
- [67] B. P. Abbott *et al.* (LIGO Scientific Collaboration and Virgo Collaboration), *Astrophys. J. Lett.* **896**, L44 (2020).
- [68] T. E. Riley *et al.*, *Astrophys. J. Lett.* **887**, L21 (2019).
- [69] M. C. Miller *et al.*, *Astrophys. J. Lett.* **887**, L24 (2019).
- [70] J. M. Lattimer and Y. Kim, *Astrophys. J.* **771**, 51 (2013).
- [71] G. Grams, A. M. Santos, P. K. Panda, C. Providência, D. P. Menezes, *Phys. Rev. C* **95**, 055807 (2017).
- [72] F. Ji, J. N. Hu, S. S. Bao, and H. Shen, *Phys. Rev. C* **102**, 015806 (2020).

- [73] B. A. Nikolaus, T. Hoch, and D. G. Madland, *Phys. Rev. C* **46**, 1757 (1992).
- [74] J. J. Rusnak and R. J. Furnstahl, *Nucl. Phys. A* **627**, 495 (1997).
- [75] T. Bürvenich, D. G. Madland, J. A. Maruhn, and P.-G. Reinhard, *Phys. Rev. C* **65**, 044308 (2002).
- [76] G. Watanabe, K. Sato, K. Yasuoka, and T. Ebisuzaki, *Phys. Rev. C* **68**, 035806 (2003).
- [77] L. W. Chen, C. M. Ko, and B. A. Li, *Phys. Rev. C* **76**, 054316 (2007).
- [78] T. Nikšić, D. Vretenar, and P. Ring, *Phys. Rev. C* **78**, 034318 (2008).
- [79] J. Daoutidis and P. Ring, *Phys. Rev. C* **80**, 024309 (2009).
- [80] P. W. Zhao, Z. P. Li, J. M. Yao, and J. Meng, *Phys. Rev. C* **82**, 054319 (2010).
- [81] S. E. Agbemava, A. V. Afanasjev, D. Ray, and P. Ring, *Phys. Rev. C* **89**, 054320 (2014).
- [82] Q. S. Zhang, Z. M. Niu, Z. P. Li, J. M. Yao, and J. Meng, *Front. Phys.* **9**, 529 (2014).
- [83] S. E. Agbemava, A. V. Afanasjev, T. Nakatsukasa, and P. Ring, *Phys. Rev. C* **92**, 054310 (2015).
- [84] P. W. Zhao and Z. P. Li, *Int. J. Mod. Phys. E* **27**, 1830007 (2018).
- [85] S. S. Bao, J. N. Hu, Z. W. Zhang, and H. Shen, *Phys. Rev. C* **90**, 045802 (2014).
- [86] F. J. Fattoyev, C. J. Horowitz, J. Piekarewicz, and G. Shen, *Phys. Rev. C* **82**, 055803 (2010).
- [87] C. J. Horowitz and J. Piekarewicz, *Phys. Rev. Lett.* **86**, 5647 (2001).
- [88] J. Carriere, C. J. Horowitz, and J. Piekarewicz, *Astrophys. J.* **593**, 463 (2003).
- [89] T. Maruyama, T. Tatsumi, D. N. Voskresensky, T. Tanigawa, and S. Chiba, *Phys. Rev. C* **72**, 015802 (2005).
- [90] B. Y. Sun, Z. W. Liu, and R. Y. Xing, *AIP Conf. Proc.* **2127**, 2127, 020020 (2019).
- [91] Z. Zhang and L. W. Chen, *Phys. Lett. B* **726**, 234 (2013).
- [92] G. Baym, C. Pethick, and P. Sutherland, *Astrophys. J.* **170**, 299 (1971).
- [93] H. Shen, F. Ji, J. N. Hu, and K. Sumiyoshi, *Astrophys. J.* **891**, 148 (2020).
- [94] F. J. Fattoyev, C. J. Horowitz, J. Piekarewicz, and B. Reed, *Phys. Rev. C* **102**, 065805 (2020).
- [95] P. B. Demorest, T. Pennucci, S. M. Ranson, M. S. E. Roberts, and J. W. T. Hessels, *Nature (London)* **467**, 1081 (2010).
- [96] E. Fonseca *et al.*, *Astrophys. J.* **832**, 167 (2016).
- [97] Z. Arzoumanian *et al.*, *Astrophys. J. Suppl.* **235**, 37 (2018).
- [98] J. Antoniadis *et al.*, *Science* **340**, 6131 (2013).
- [99] H. T. Cromartie *et al.*, *Nat. Astron.* **4**, 72 (2020).